Philosophical Magazine,
Vol. 86, No. 24, 21 August 2006, 3757–3778

Taylor & Francis
Taylor & Francis Group

Polycrystalline patterns in far-from-equilibrium freezing: a phase field study

L. GRÁNÁSY*†, T. PUSZTAI†, T. BÖRZSÖNYI†, G. I. TÓTH†, G. TEGZE†, J. A. WARREN‡ and J. F. DOUGLAS‡

†Research Institute for Solid State Physics and Optics, H-1525 Budapest, POB 49, Hungary
‡National Institute of Standards and Technology, Gaithersburg, MD 20899, USA

(*Received 1 February 2005; in final form 28 April 2005*)

We discuss the formation of polycrystalline microstructures within the framework of phase field theory. First, the model is tested for crystal nucleation in a hard sphere system. It is shown that, when evaluating the model parameters from molecular dynamics simulations, the phase field theory predicts the nucleation barrier for hard spheres accurately. The formation of spherulites is described by an extension of the model that incorporates branching with a definite orientational mismatch. This effect is induced by a metastable minimum in the orientational free energy. Spherulites are an extreme example of polycrystalline growth, a phenomenon that results from the quenching of orientational defects (grain boundaries) into the solid as the ratio of the rotational to the translational diffusion coefficient is reduced, as is found at high undercoolings. It is demonstrated that a broad variety of spherulitic patterns can be recovered by changing only a few model parameters.

1. Introduction

Many of the structural materials in use are polycrystalline, i.e. they are composed of a large number of crystallites, whose size, shape, and composition distributions determine their properties and failure characteristics. The size scale of the constituent crystal grains ranges from a few nanometres to centimetres in different classes of materials. The formation of polycrystalline matter is generally poorly understood. For example, little is known of the initial fluctuation-driven formation of crystallites, *nucleation*, especially when heterogeneities (foreign particles, walls) are involved in the process. While nucleation takes place on the nanometer scale, its influence extends to larger size scales. Controlled nucleation [1] is an established tool for tailoring the microstructure of matter for specific applications. The enormous morphological richness of polycrystalline structures observed in thin polymer layers reflects the complexity of polycrystalline freezing, and gives important clues to the

*Corresponding author. Email:grana@szfki.hu

Philosophical Magazine
ISSN 1478–6435 print/ISSN 1478–6443 online © 2006 Taylor & Francis
http://www.tandf.co.uk/journals
DOI: 10.1080/14786430500198569

mechanisms that govern their formation. Polycrystalline patterns have also biological relevance: semi-crystalline spherulites of amyloid fibrils are found in association with Alzheimer and Creutzfeldt–Jakob diseases, type II diabetes, and a range of systemic and neurotic disorders [2].

Polycrystalline materials can be divided into the following three classes (see figure 1):

(a) Polycrystalline structures formed by impinging single crystals.
(b) Polycrystalline growth forms, where new grains of different crystallographic orientations form at the perimeter of the particle.
(c) Structures formed by impinging polycrystalline particles.

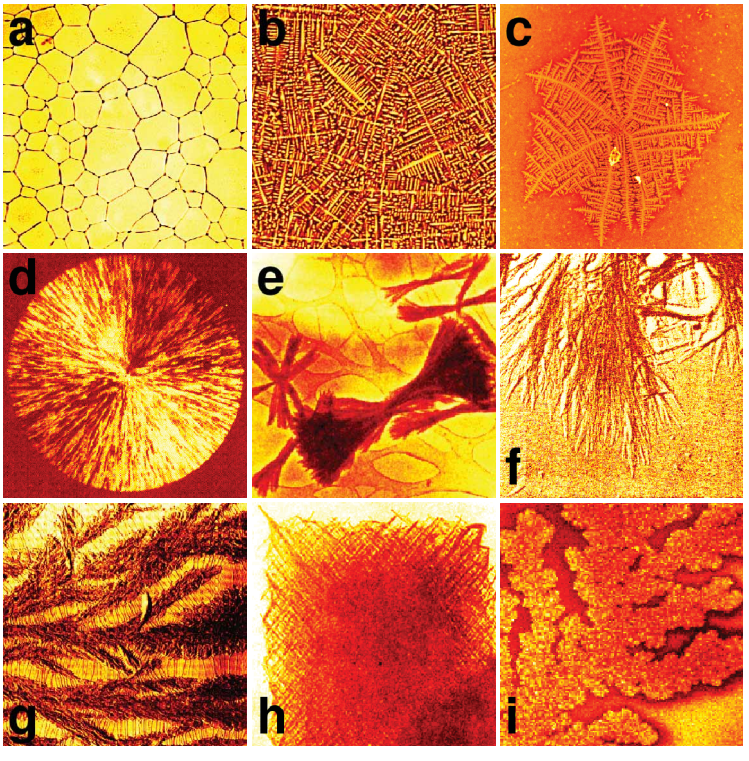

Figure 1. Polycrystalline patterns. *Impinging single crystals:* (a) Foam-like morphology formed by competing nucleation and growth [3]. (b) Polycrystalline dendritic structure formed by competing nucleation and growth in the oxide glass $(ZnO)_{61.4} \cdot (B_2O_3)_{38.6} \cdot (ZnO_2)_{28}$ [4]. *Nucleation at the perimeter*: (c) 'Dizzy' dendrite formed in clay filled polymethyl methacrylate–spolyethylene oxide thin film [5, 6]. (d) Spherulite formed in pure Se [7]. (e) Crystal sheaves in pyromellitic dianhydrite–oxydianilin poly(imid) layer [8] (f) Arboresque growth form in polyglycine [9]. (g) Polyethylene spherulite crystallized in the presence of n-paraffin [10]. (h) 'Quadrite' formed by nearly rectangular branching in isotactic polypropylene [11]. (i) Fractal-like polycrystalline aggregate of electrodeposited Cu [12]. To improve the contrast/visibility of the experimental pictures, they are shown here in false colour.

Crystal nucleation plays a central role in the formation of all these structures. Following a terminology widely used by the polymer community, we distinguish *primary* and *secondary* nucleation of crystallites. *Primary nucleation* produces individual single crystals or growth centres. *Secondary nucleation*, in turn, produces new crystal grains at the perimeter of existing particles. Both these processes may be induced by the internal fluctuations of the system (*homogeneous* process) or by foreign particles (*heterogeneous* process). The micro-mechanism of the homogeneous secondary nucleation as yet needs identification/clarification, though it is expected that crystallographic branching, which happens in directions favoured by grain boundary energy minima, may play an important role.

Considering these distinct modes of nucleation, a general theory of polycrystalline solidification needs to incorporate the following minimal ingredients:

(i) Diffusional instabilities;
(ii) Primary nucleation (homogeneous and heterogeneous); and
(iii) Secondary nucleation (homogeneous and heterogeneous, random branching included).

The phase field theory proved a very successful approach in describing complex crystallization morphologies [13–15]. Such a field theoretic formulation provides a promising starting point for developing a general model of polycrystalline freezing especially in the light of recent developments in phase field modelling of crystal nucleation briefly reviewed next.

Homogeneous primary nucleation: Nucleation is traditionally modelled in the phase field theory by adding Langevin noise terms to the equation of motion. Such an approach has been used for describing homogeneous nucleation in single-component [16] and binary alloy systems [17], and during eutectic solidification in binary models [18–20].

Besides performing simulations of the nucleation process, the phase field approach can also be used to *calculate the features of the critical fluctuations* [17, 21]. This includes the determination of the order parameter profiles and the height of the nucleation barrier. In a few cases, *all parameters of the phase field theory can be fixed*, and such calculations can be performed without adjustable parameters. For example, in the one-component limit, the free energy functional contains only two parameters, the coefficient of the square-gradient term for phase field and the free energy scale (height of the central hill between the double well in the local free energy density). If the thickness and the free energy of a crystal–liquid interface are known for the equilibrium crystal–liquid interface, all model parameters can be fixed and the properties of the critical fluctuation, including the height of the nucleation barrier, can be predicted without adjustable parameters. Such information is available from atomistic simulations/experiments for a few cases (Lennard–Jones system and ice–water system). This procedure leads to a good quantitative agreement with the magnitude of the nucleation barriers deduced from atomistic simulations for the Lennard–Jones system, and from experiments on ice nucleation in undercooled water [17]. Similar results have been obtained for the hard-sphere system using a phase field model that relies on a structural order parameter coupled to the density field [22]. Again, the model parameters have been fixed via the interface thickness and interfacial free energy

from atomistic simulations, so the calculations were performed without adjustable parameters.

Heterogeneous primary nucleation: Recently, steps have been made towards a physical modelling of heterogeneous nucleation within the phase field theory. Castro [6] introduced walls (boundaries) into a single-order parameter theory by assuming a no-flux boundary condition at the interface ($\mathbf{n}\nabla\phi = 0$, where $\mathbf{n}$ is the normal vector of the wall), which results in a contact angle of 90° at the wall–solid–liquid triple junction. Langevin noise is then introduced to model nucleation. We generalized this approach to the nucleation of crystallites with different crystallographic orientation in a binary system [15]. Prescribing $(\mathbf{n}\nabla\phi) = 0$ and $(\mathbf{n}\nabla c) = 0$ at the wall perimeter, we introduce chemically inert surfaces, and perform simulations to address heterogeneous volume nucleation on foreign particles, on rough surfaces, and in confined space (porous matter and channels).

Homogeneous secondary nucleation: Polycrystalline patterns that grow by producing new crystal grains at the perimeter have been observed in liquids without particulates or detectable molecular impurities. Considering the observations of Magill [23], who noted that spherulites only seem to appear in highly undercooled pure fluids of sufficiently large viscosity, we hypothesize that the decoupling of the translational and rotational diffusion coefficient observed in such systems is responsible for the propensity for polycrystalline growth in highly undercooled liquids. Specifically, a reduced D_{rot} should make it difficult for newly forming crystal regions to reorient with the parent crystal to lower its free energy at the growth front that is advancing with a velocity scaling with the translational diffusion coefficient D_{tr}. Thus, epitaxy cannot keep pace with solidification, and consequently the orientational order that freezes in is incomplete. This *trapping of orientational disorder* can be captured within the phase field theory by reducing the orientational mobility while keeping the phase field mobility constant as discussed in detail by Gránásy *et al*. [15, 24]. Specifically, in our model the growth velocity scales linearly with M_ϕ, so consistency requires $M_\phi \propto D_{\mathrm{tr}}$. Since we also expect that $M_\theta \propto D_{\mathrm{rot}}$, the difference in the temperature dependences of the translational and rotational diffusion coefficients can be modelled by changing the ratio M_θ/M_ϕ.

Heterogeneous (particle-induced) secondary nucleation: The formation of the new grains at the interface might be induced by the foreign particles floating in the liquid. We have recently developed two methods to incorporate them: insertion of orientation pinning centres, areas of random but fixed orientation, Gránásy *et al*. [25]; and introduction of particles of 90° contact angle as described above [15].

Experiments on polymeric systems indicate an additional mechanism of homogeneous secondary nucleation, which we term here *random crystallographic branching* and produces new grains of well-defined orientational relationship with the initial grain at the growth front.

In this paper, we formulate a general model of polycrystalline freezing that incorporates all the primary and secondary nucleation modes mentioned above, including random crystallographic branching, and address the formation of diverse polycrystalline growth patterns.

2. Phase field theory for polycrystalline solidification

We start from a phase field theory of polycrystalline solidification by Gránásy *et al*. [17], which has been modified to incorporate foreign particles [25], and is able to describe primary and secondary nucleation in two dimensions [15, 24]. The mechanism of *random crystallographic branching*, is a new feature that has now been incorporated, as described below.

In our approach, the local phase state of matter (solid or liquid) is characterized by the phase field ϕ (a structural order parameter). Other basic field variables are the solute concentration c, and the normalized orientation field θ that specifies the orientation of crystal planes in the laboratory frame. Note that in two dimensions a single orientation angle suffices, and that this formulation of the theory is valid for two dimensions or for quasi-two-dimensional objects such as thin films. A true three-dimensional formulation, in contrast, needs minimum three fields to describe crystallographic orientation. Work is underway to develop a three-dimensional generalization of the polycrystalline phase field theory [26, 27].

The free energy in the present two-dimensional formulation consists of several contributions that will be discussed next:

$$F=\int d^2r\left\{\frac{\varepsilon_\phi^2 T}{2}s^2(\vartheta,\theta)|\nabla\phi|^2+w(c)Tg(\phi)+[1-p(\phi)]f_s(c,T)+p(\phi)f_l(c,T)+f_{\mathrm{ori}}(|\nabla\theta|)\right\}, \tag{1}$$

where

$$\begin{aligned} w(c) &= (1-c)w_A + cw_B, \\ g(\phi) &= \tfrac{1}{4}\phi^2(1-\phi)^2,\ g'(\phi) = \phi^3 - \tfrac{3}{2}\phi^2 + \tfrac{1}{2}\phi \\ p(\phi) &= \phi^3(10-15\phi+6\phi^2),\ p'(\phi) = 30\phi^2(1-\phi)^2, \\ s(\vartheta,\theta) &= 1+s_0\cos\left[k\left(\vartheta-\frac{2\pi\theta}{k}\right)\right],\ \vartheta = \arctan\left[\frac{(\nabla\phi)_y}{(\nabla\phi)_x}\right] \end{aligned}$$

Here ε_ϕ is the coefficient of the square-gradient term for the field ϕ, w_i is the free energy scale for the ith pure component ($i=A,B$), s, g, and p are the anisotropy function, the quartic double-well function, and the interpolation function. ϑ is the inclination of the normal vector of the interface in the laboratory frame. s_0 is the amplitude of the anisotropy of the interface free energy, while k is the symmetry index ($k=6$ for sixfold symmetry). The square gradient-term is responsible for the diffuse interface appearing in the model, while $f_s(c,T)$ and $f_l(c,T)$ are the composition and temperature dependent free energy densities in the bulk solid and liquid phases, respectively, that provide the driving force for solidification.

The present model differs from previous versions used by Gránásy *et al*. [17, 24, 25] in the form of the orientational contribution f_{ori} to the free energy density that represents the excess free energy density due to inhomogeneities in crystal orientation in space, in particular, the misorientation due to a grain boundary.

It is now modified so that preferred crystallographic misfits appear in the model.

$$f_{\mathrm{ori}} = [1 - p(\phi)]\frac{HT}{2\xi_0}\left\{xF_0 + (1-x)F_1\right\}$$
$$F_0 = \begin{cases} \left|\sin(2\pi m\xi_0|\nabla\theta|)\right| & \text{for} \quad \xi_0|\nabla\theta| < \dfrac{3}{4m} \\ 1 & \text{otherwise} \end{cases} \tag{2}$$
$$F_1 = \begin{cases} \left|\sin(2\pi n\xi_0|\nabla\theta|)\right| & \text{for} \quad \xi_0|\nabla\theta| < \dfrac{1}{4n} \\ 1 & \text{otherwise} \end{cases}$$

Here H sets the value of the small angle grain boundaries, and ξ_0 is the correlation length of the orientation field. The orientation field extends into the liquid, where it is made to fluctuate in time and space. Local temporary value of the orientation field in the liquid is understood as follows. Due to geometrical and/or chemical constraints, a short-range order exists even in simple liquids, which is often similar to the short-range order in the solid. Rotating the crystalline first-neighbour shell so that it aligns optimally with the local liquid structure, one can assign a local orientation to every atom in the liquid. The orientation obtained in this manner fluctuates in time and space. The correlation of the atomic positions/angles shows how good this fit is. (In the model, the fluctuating orientation field and the phase field play these roles.) Approaching the solid from the liquid, the orientation becomes more definite (the amplitude of the orientational fluctuations decreases) and matches to that of the solid, while the correlation between the local liquid structure and the crystal structure improves. In the present model, the orientation field and the phase field are strongly coupled to recover this behaviour.

This form of f_{ori} ensures that θ takes an essentially constant value (scaled between 0 and 1) in the solid, while in the liquid it fluctuates. The latter feature reflects the local order in the liquid. Orientational ordering takes place at the diffuse interface simultaneously with the structural transition. The orientational free energy has two local minima as a function of the angle $\xi_0|\nabla\theta|$, corresponding to no misorientation and a preferred misorientation (figure 2). This means that regions with large enough orientation difference from a neighbouring parent crystal will relax towards a finite misorientation. This selection of grain orientation only occurs provided that noise does not disrupt the process. The branching angle and the depth of this metastable minimum of f_{ori} are specified by m, n, and x. In any real system, there will be many preferred (low energy) orientations, a reflection of the underlying crystallographic symmetries. In our illustrative calculations $n = \frac{1}{2}$ has been set, while $m = 1, 2$, and 3 correspond to branching with 90, 45, and 30°, respectively. We note that, with appropriate choice of the parameters ($x = 0$), the orientational preference by the metastable free energy minimum can be removed.

The orientational contribution to the free energy is multiplied with $1 - p(\phi)$ to avoid double counting the orientational contribution in the liquid, which is *per definitionem* incorporated into the free energy of the bulk liquid. With appropriate choice of the model parameters, an ordered liquid layer surrounds the crystal as seen in atomistic simulations. With such a choice, double counting of the orientational contribution to the interfacial free energy is also avoided, and the relations between

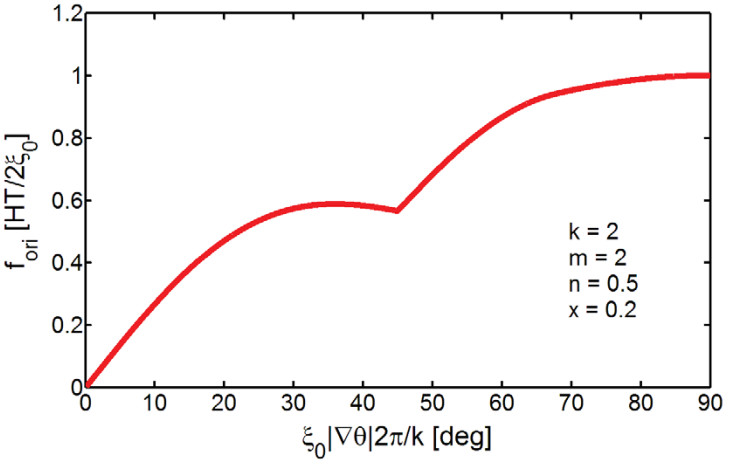

Figure 2. Orientational free energy f_{ori} as a function of misorientation angle (in degree) for two-fold symmetry ($k=2$), while $n=\frac{1}{2}$, $m=2$, and $x=0.2$. If the neighbouring pixel has a smaller misorientation than $\sim 36^\circ$ (local maximum), it can reduce the free energy by relaxing to the bulk crystal orientation (0°). If misorientation is larger than this, the closest minimum is 45°. So, neighbouring pixels of large misorientation tend to relax to 45°, unless fluctuations prevent this. Note that θ is an angular variable, so the maximum possible misorientation is $\Delta\theta_{\max}=0.5$.

the model parameters ε_ϕ and w_i and the measurable interfacial properties of the constituent elements,

$$\varepsilon_\phi^2 = \frac{6\sqrt{2}\gamma_i\delta_i}{T_i} \quad \text{and} \quad w_{A,B} = \frac{12\gamma_i}{\sqrt{2}\delta_i T_i}, \tag{3}$$

remain unchanged in the presence of the orientation field. Here γ_i, δ_i, and T_i are the interfacial free energy, the interface thickness, and the melting point for the ith pure component ($i=A, B$).

Time evolution is governed by relaxational dynamics and noise terms are added to model thermal fluctuations,

$$\begin{aligned}
\dot{\phi} &= -M_\phi \frac{\delta F}{\delta \phi} + \zeta_\phi = M_\phi \left\{ \nabla\left(\frac{\partial I}{\partial \nabla \phi}\right) - \frac{\partial I}{\partial \phi} \right\} + \zeta_\phi \\
\dot{c} &= \nabla M_c \nabla\left(\frac{\delta F}{\delta c} - \zeta_j\right) = \nabla\left\{ \frac{v_m}{RT} Dc(1-c) \nabla\left[\left(\frac{\partial I}{\partial c}\right) - \nabla\left(\frac{\partial I}{\partial \nabla c}\right) - \zeta_j \right] \right\} \\
\dot{\theta} &= -M_\theta \frac{\delta F}{\delta \theta} + \zeta_\theta = M_\theta \left\{ \nabla\left(\frac{\partial I}{\partial \nabla \theta}\right) - \frac{\partial I}{\partial \theta} \right\} + \zeta_\theta
\end{aligned} \tag{4}$$

where I is the total free energy density (including the gradient terms), v_m is the molar volume, D the diffusion coefficient in the liquid, and ξ_i are the appropriate noise terms.

The time scales for the three fields are determined by the mobility coefficients appearing in the coarse-grained equations of motion: M_ϕ, M_c, and M_θ. The mobility, M_c, is directly proportional to the classic interdiffusion coefficient for a

binary mixture. The mobility M_ϕ dictates the rate of crystallization, while M_θ controls the rate at which regions reorient. In the simulations, we use an anisotropic mobility for the phase field $M_\phi \propto 1 + \delta_0 \cos[k(\vartheta - 2\pi\theta/k)]$, where k and ϑ have the same meaning as in the anisotropy function for the interfacial free energy, while δ_0 is the anisotropy parameter. The equations of motion are detailed elsewhere [15, 17].

Gaussian white noises of amplitude $\zeta = \zeta_s + (\zeta_l - \zeta_s)\, p(\phi)$ have been added to the non-conserved fields, where ζ_l and ζ_s are the amplitudes in the liquid and solid. The noise has been discretised as described by Karma and Rappel [28] and Plapp [29]. The noise amplitude scales with the spatial and time steps, with the temperature and the film thickness as follows:

$$\zeta' = \zeta\left(\frac{\Delta x}{\Delta x'}\right) \times \left(\frac{\Delta t'}{\Delta t}\right)^{1/2} \times \left(\frac{T'}{T}\right)^{1/2}, \tag{5}$$

where the primed quantities are for the actual simulation, and those without prime belong to a reference state, in which the noise amplitude was ζ.

In the case of conserved concentration field, a random flux has been added to the equation of motion as described by Karma and Rappel [28].

2.1. *Numerical solution*

The governing equations have been solved numerically using an explicit finite difference scheme. The size of the rectangular grid has been varied between 500×500 and 5000×5000. Periodic boundary conditions have been applied. The time and spatial steps were chosen to ensure stability of the solutions. As the computed morphologies are fundamentally determined by thermal fluctuations at the growth front, convergence to a particular morphology, as we refine the grid and time step, is possible only in a statistical sense (i.e., the rate of secondary nucleation, and the solid fraction inside the solidification envelopes). We note that accurate solutions to the orientation equation require approximately 1/50 of the time step required for the stable solution of the other fields.

A parallel code has been developed that relies on the Message Passing Interface (MPI) protocol and was run on a PC cluster built up at the Research Institute for Solid State Physics and Optics, Budapest, exclusively for phase field calculations. This cluster consists of 80 nodes and a server machine. The present paper is based on computations exceeding 40 CPU-years on a 2 GHz processor.

2.2. *Primary nucleation*

In order to demonstrate the accuracy of the phase field theory in describing crystal nucleation, we perform an extended analysis in a case (crystal nucleation in the one-component hard-sphere liquid) where all the model parameters can be fixed and the properties of the critical fluctuations are known from atomistic simulations.

As the critical fluctuation is in an unstable equilibrium with the initial liquid, it represents an extremum of the free energy functional, which is subject to conservation constraints when the phase field is coupled to conserved fields such as solute concentration or energy. Such constraints are imposed by the method of

Lagrange multipliers. The field distributions, that extremize the free energy, obey the appropriate Euler–Lagrange equations,

$$\frac{\delta F}{\delta \psi_i} = \frac{\partial I}{\partial \psi_i} - \nabla \frac{\partial I}{\partial \nabla \psi_i} = 0, \tag{6}$$

where $\delta F/\delta \psi_i$ stands for the first functional derivative of the free energy with respect to the field ψ_i, while I is now the constrained free energy density (including the terms with the Lagrange multipliers). Here ψ_i stand for all the fields (conserved and non-conserved) used in theory. These equations are solved assuming that unperturbed liquid exists in the far field, while, for symmetry reasons, zero field gradients exist at the centre of the fluctuations. This solution can also be obtained as the nontrivial time-independent solution of the governing equations for field evolution. The work of formation of the nucleus (height of the nucleation barrier) can now be obtained by inserting the solution into the free energy functional. Herein we present an extended test of theory for the hard-sphere system.

3. Materials and simulation parameters

For specificity, we employ the well-studied, ideal solution phase diagram of the Ni–Cu alloy (for the relevant properties see [30]). This choice is not particularly restrictive, as it is formally equivalent to a pure material [30], where thermal diffusion replaces solute diffusion as the dominant transport mechanism. Moreover, the model is in no way restricted to metals as our application to polymer materials below demonstrates. We fix the temperature to be 1574 K, as in previous studies. The orientation dependence of the molecular attachment kinetics is modelled via an anisotropic dimensionless phase field mobility. The fibre-like crystallites that form in many polymeric materials imply a twofold symmetry ($k = 2$) and a large kinetic anisotropy, which was chosen as $\delta_0 = 0.995$. A similar anisotropy function has been used for the interfacial free energy, $\gamma = \gamma_0$. Crystal growth is sensitive to both kinetic and interfacial free energy anisotropies, where increasing either yields sharper needle crystal morphologies. The calculations were performed with *supersaturations* S in the range of $0.75 \leq S = (c_L - c)/(c_L - c_S) \leq 1.2$, where $c_L = 0.466219$, $c_S = 0.399112$, and c are the concentrations at the liquidus, solidus, and the initial homogeneous liquid mixture, respectively.

Since the physical thickness of the interface is in the nanometer range and the typical solidification structures are far larger (μm to mm), a full simulation of polycrystalline solidification from nucleation to particle impingement cannot be performed even with the fastest of the present supercomputers without substantial algorithmic improvement. Such improvements are an active area of research. Since we seek here a qualitative understanding, following other authors ([30, 31]), the interface thickness has been increased (by a factor of 20.8), the interface free energy has been reduced (by a factor of 6), while the diffusion coefficient has been increased (by a factor of 100). This allows us to follow the life of crystallites from birth to impingement on each other.

The non-dimensionalisation of the equations of motion has been done using the length and time scales ξ and ξ^2/D_l, where D_l is the diffusion coefficient in

the liquid. In the computations, we used $\xi = 2.1 \times 10^{-4}$ cm and $D_l = 10^{-5}$ cm^2/s. The dimensionless time and spatial steps were chosen as $\Delta t = 4.75 \times 10^{-6}$ and $\Delta x = 6.25 \times 10^{-3}$, while the reduced correlation length of the orientation field was assumed to be $\xi_0/\xi = \Delta x$ (corresponding to $\sim$13 nm). Dimensionless mobilities of $m_\phi = m_{\phi,0}\{1 + \delta_0 \cos[k(\vartheta - 2\pi\theta/k)]\}$, $m_c = m_{c,S} + (m_{c,L} - m_{c,S})p(\phi)$, and $m_\theta = m_{\theta,S} + (m_{\theta,L} - m_{\theta,S})p(\phi)$ have been used for the phase-, concentration-, and orientation fields, respectively. Unless stated otherwise, we applied $m_{\phi,0} = M_\phi \alpha_0^2 T/D_l = 1.0$, $m_{c,L} = (RT/v_m)D_l c(1-c)$, $m_{c,S} = 0$, $m_{\theta,L} = M_{\theta,L}\xi HT/D_l = 360$, and $m_{\theta,S} = M_{\theta,S}\xi HT/D_l = 0$.

4. Results and discussion

First, we demonstrate that the present model gives a reasonable description of the individual primary and secondary nucleation modes needed in a general case. We then address the form and growth of spherulites that are the most prominent representatives of complex polycrystalline structures forming in highly non-equilibrium liquids, and show an amazing morphological variability.

4.1. *Homogeneous primary nucleation*

Recent developments in atomistic modelling of small crystalline clusters in the hard-sphere system allow for an extension of the quantitative analysis described by Gránásy *et al*. [22]. Cacciuto *et al*. [32] evaluated the free energy of clusters in the hard-sphere liquid of equilibrium density as function of size that allowed the determination of the size dependence of the solid–liquid interface free energy. The results extrapolate to $\gamma_{R\to\infty} = 0.616(3)\, kT/\sigma^2$, the cluster average of the interfacial free energy for infinite size (σ is diameter of the hard spheres). This value agrees well with results from molecular dynamics simulations (e.g. with $\gamma_{\rm av}/(kT/\sigma^2) = 0.612 \pm 0.02$ for the average of the values for the (111), (110), and (100) directions by Davidchack and Laird [33]; and with $\gamma_{\rm av}/(kT/\sigma^2) = 0.63 \pm 0.02$ by Mu *et al*. [34]). This allows the fixing of the coefficient of the square-gradient term with a higher accuracy than in previous work, since it was uncertain how far the cluster (or orientational) average of the interfacial free energy falls from the average for the (111), (110), and (100) directions. A further refinement of the theory is that the density dependence of the coefficient of the square-gradient term, $\varepsilon_\phi^2 \propto d^2C(k)/{\rm d}k^2$, and of the free energy scale, $w \propto 1/S(k)$, are taken into consideration, where $C(k)$ is the direct correlation function of the liquid which is related to the structure factor of the liquid via $S(k) = 1/[1 - C(k)]$.

The parameter-free predictions of the PFT and the exact Monte Carlo (MC) results are compared in figure 3. The agreement between theory and MC simulations is convincing; considerably better than the (also parameter-free) predictions of the classical nucleation theory. The uncertainty of the input data (interfacial free energy, equations of state, etc.) does not influence this result perceptibly [35].

These findings suggest that, using the physical interface thickness, the phase field theory is able to predict the height of the nucleation barrier quantitatively. This success, together with the parameter-free prediction of the dendritic growth rate [14], suggests that a multiscale approach to the phase field theory with model

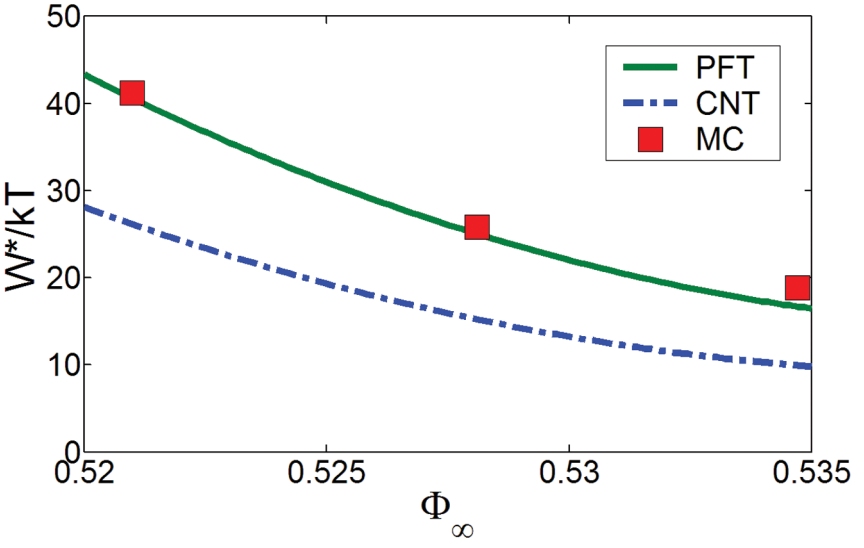

Figure 3. Homogeneous primary nucleation. The height of the nucleation barrier vs. the initial density of the hard-sphere liquid as predicted by the phase field theory (PFT), the sharp interface droplet model of the classical nucleation theory (CNT). These calculations contain no adjustable parameters. For comparison the height of the nucleation barrier from Monte Carlo (MC) simulations is also presented [36].

parameters deduced from atomistic simulations is capable of quantitative predictions for both crystal nucleation and growth.

Homogeneous primary nucleation is incorporated into our model via adding noise to the governing equations. This method has been analysed in detail by Castro [16].

4.2. *Heterogeneous primary nucleation*

We performed phase field simulations to model primary heterogeneous nucleation on particles and rough surfaces, and solidification in porous medium in two (figure 4) and three dimensions (figure 5). In the three dimensional calculations, a simpler phase field model has been used, that neglects the differences in crystallographic orientation. The latter model has been used to explore primary heterogeneous nucleation on a stair-like surface, in a porous medium (represented by cubes placed on a bcc lattice), and on a three-dimensional checkerboard-like modulated surface (figure 5). Such studies might contribute to a better understanding of processes that can be used in micro/nano-patterning. A detailed analysis of this method in 2D has been presented by Castro [16].

4.3. *Heterogeneous secondary nucleation*

Foreign particles may induce polycrystalline growth. For example, a disordered dendritic structure termed a 'dizzy' dendrite (figure 6) forms by the engulfment of the clay particles into the crystal, inducing the formation of new grains [5, 6]. This phenomenon is driven by the impetus to reduce the crystallographic misfit

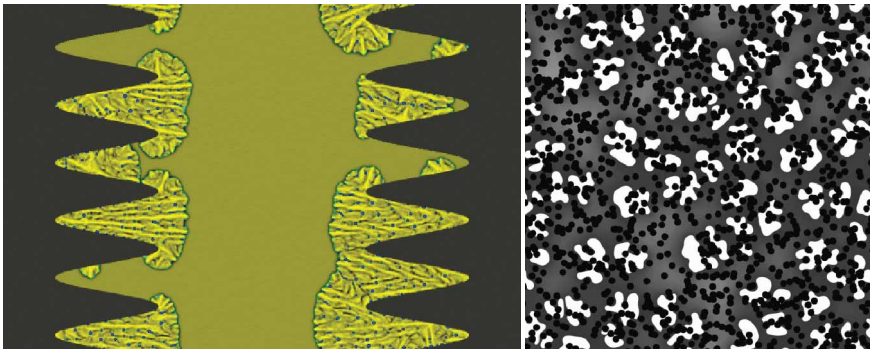

Figure 4. Heterogeneous primary nucleation in two dimensions: on rough surfaces (left) and on foreign particles (right). Note that nucleation happens in the 'notches' of the foreign surfaces. Composition fields are shown (white — solidus, dark grey — liquidus, black — foreign matter/walls).

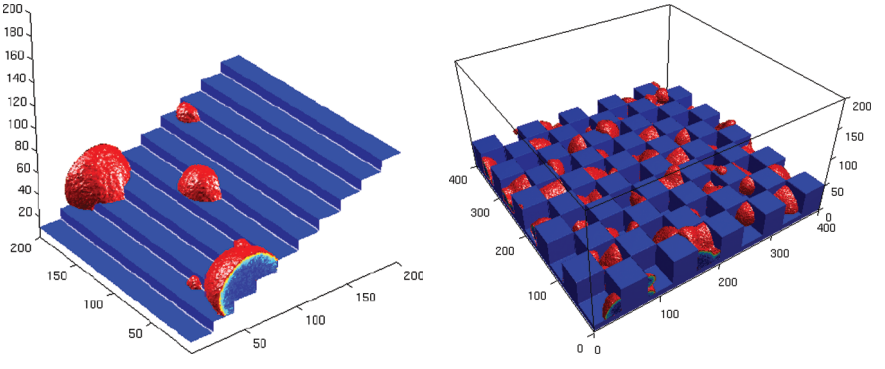

Figure 5. Heterogeneous primary nucleation in three dimensions: on stairs (left) and on a checkerboard-modulated surface (right).

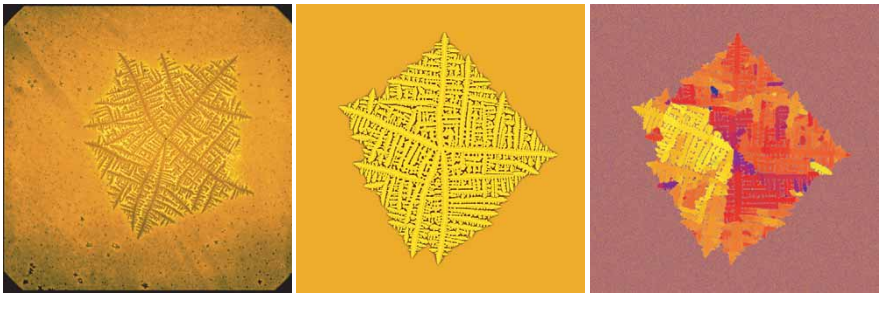

Figure 6. 'Dizzy' dendrite in experiment (left) and phase field simulation (composition: centre; orientation: right).

along the perimeter of clay particles by creating grain boundaries within the polymer crystal. This process changes the crystal orientation at the dendrite tip, changing thus the tip trajectory ('tip deflection'). To describe this phenomenon, Gránásy *et al*. [25] incorporated a simple model of foreign crystalline particles into the phase field theory: They are represented by *orientation pinning centres* — small areas of random, but fixed orientation — which are assumed to be of a foreign material, and not the solid $\phi = 0$ phase. This picture economically describes morphological changes deriving from particle–dendrite interactions. Using an appropriate density of pinning centres, comparable to the density of clay particles, a striking similarity is obtained between experiment and simulation (figure 6). This description extends to such fine details as curling of the main arms and the appearance of extra arms. The disorder in the dendritic morphology reflects the underlying polycrystalline structure that emerges as dendrite tips deflect on foreign particles. Increasing the number density of the foreign particles, a gradual transition is observed between the single crystal symmetric dendrite and a polycrystalline seaweed structure (figure 7, upper row). The latter morphology is observed in the case of single crystals when the anisotropy is small. Here the seaweed morphology forms due to the randomization of the orientation caused by the small crystallites, which restores isotropy at large scales. A more detailed analysis of this mode of secondary nucleation has been presented by Gránásy *et al*. [15, 24, 25].

4.4. *Homogeneous secondary nucleation*

(*a*) *Trapping of incomplete orientational ordering*: We have performed a systematic study of polycrystalline morphologies formed by reducing the orientational mobility while keeping the phase field mobility constant. The reference value of M_θ/M_ϕ has been selected to be large enough to ensure single crystal growth. When M_θ/M_ϕ is sufficiently small, the system can no longer establish the same orientation along the perimeter of the growing crystal, as suggested by our initial hypothesis. This homogeneous mechanism of secondary nucleation gives rise to a transition to polycrystalline growth (figure 7, lower row). We observed that homogeneous and heterogeneous secondary nucleation lead to strikingly similar morphologies and grain structures (figure 7). These findings demonstrate a duality between the morphologies evolving due to the effects of static heterogeneities (foreign particles) and dynamic heterogeneities (quenched-in orientational defects). An interesting observation is that the polycrystalline seaweed structures do not show the *doublon* structure commonly seen in simulations for single crystal seaweed patterns. This finding may deserve a closer inspection as – if proven a general feature – it could serve as a criterion for deciding whether a seaweed structure is polycrystalline or not. A more detailed analysis of this mode of secondary nucleation has been presented by Gránásy *et al*. [15, 24].

(*b*) *Random crystallographic branching*: Another possible mechanism of homogeneous secondary nucleation is random crystallographic branching with fixed misorientation. This is expected if a strongly preferred branching orientation exists in the system, which then yields a random formation of new grains at the growth front whose orientations are in well-defined relationships with the parent crystal.

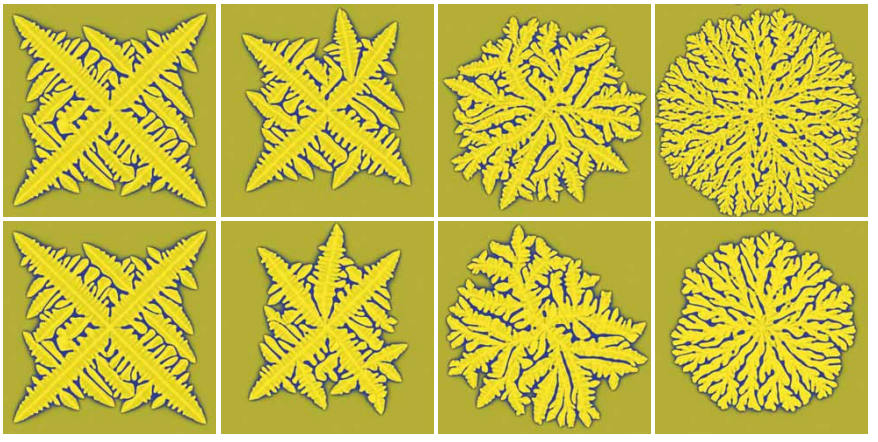

Figure 7. Dendrite to seaweed transition induced by heterogeneous (upper row) and homogeneous (lower row) secondary nucleation. (Upper row: the number of particulates increases from left to right as $N = 0$, 12 500, 50 000 and 200 000; lower row: the orientational mobility is multiplied by the factors 1, 0.4, 0.3, or 0.1. Computations were performed with the thermodynamic properties of Ni–Cu, at a supersaturation of 0.8, and on a 500×500 grid. Composition fields are shown).

As this is a mechanism newly incorporated into our phase field theory, we explore its consequences in more detail. The branching angle and the depth of the metastable minimum of f_{ori} are specified by model parameters m, n, and x. We have chosen $n = \frac{1}{2}$, and vary the other two parameters. Since this type of branching phenomenon is expected in polymeric matter that forms fibre-like elongated crystals, we assumed here a large anisotropy ($\delta_0 = 0.995$) and a two-fold symmetry of the phase field mobility ($k = 2$). We investigate the effect of these parameters on the growth patterns below systematically.

Setting the *branching angle*s to 90, 60, 45, and 30 degrees ($m = 1$, 1.5, 2, and 3), only one, two, three, and five extra orientations are allowed in the growth forms in addition to the one that nucleated, as illustrated in figure 8. Note that while the growth form produced by 90 degrees branching is rather similar to a single crystal dendrite grown at a fourfold symmetry of the interfacial free energy or phase field mobility, it has been grown with a twofold symmetry of the phase field mobility and consists of grains of two different crystallographic orientations. These results demonstrate that indeed metastable minima of the orientational free energy f_{ori} yield branching in well-defined orientations.

We find that the branching frequency increases with an increasing *depth of the metastable minimum* (figure 9), and a transition between the needle crystal and more space-filling forms is observed. With further increase of the depth of the metastable minimum, fractal-like polycrystalline aggregates consisting of small crystallites appear. A similar morphological transition has been found when increasing the *driving force* of solidification (figure 10). In contrast, increasing the *amplitude of orientational noise* reduces the propensity for branching, as the enhanced noise drives the system towards the stable minimum of f_{ori}.

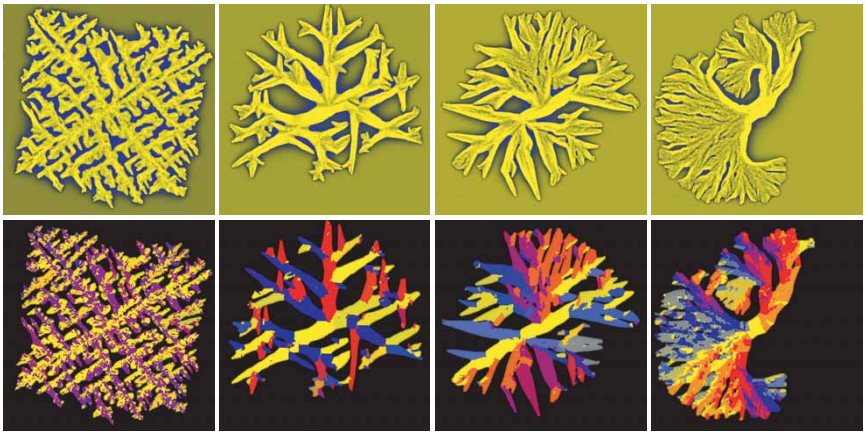

Figure 8. Polycrystalline patterns formed by *random crystallographic branching* with branching angles of 90, 60, 45, and 30°, in a system of extreme large twofold anisotropy of the phase field mobility ($\delta_0 = 0.995$). (Upper row: composition map; lower row: orientation map. Computations were performed with the thermodynamic properties of Ni–Cu, at a supersaturation that varies from left to right as 0.85, 0.95, 1.00, and 1.00. Depth of the metastable well of f_{ori} was $x = 0.2$. A 500×500 grid has been used). All patterns nucleated as a small needle crystal with its axis tilted 30° relative to the horizon.

Figure 9. Branching vs. depth of the metastable well (x) of the orientational free energy. From left to right: $x = 0.1$, 0.15, 0.2, and 0.25. Note the decreasing grain size. Other conditions are as for the rightmost column of figure 8. Upper row: composition map; lower row: orientation map.

Finally, we emphasize that mechanisms (a) and (b) discussed in this section provide two examples of homogeneous secondary nucleation. It seems highly probable that the micromechanisms of homogeneous secondary nucleation differ for the many diverse systems that display polycrystalline solidification at high undercoolings. Trapping of orientational disorder and branching with fixed misorientation might be coarse-grained representations of many of them, though probably not

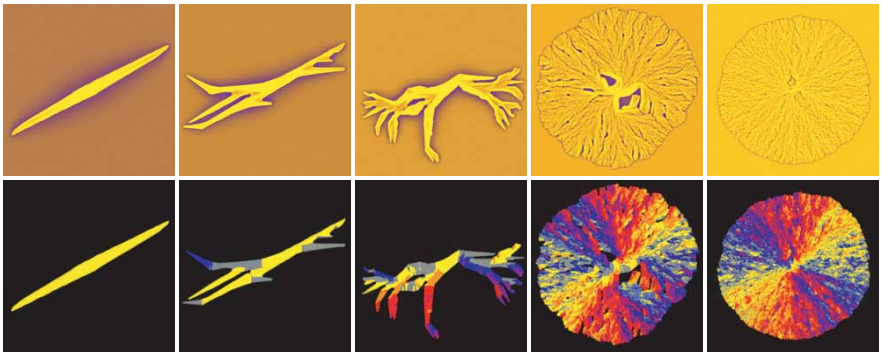

Figure 10. Polycrystalline patterns formed by random crystallographic branching as a function of supersaturation that varies as $S = 0.7$, 0.8, 0.9, 1.0, and 1.1 from left to right. The branching angle is 30°. Other conditions are as for figure 8. (Upper row: composition map; lower row: orientation map). Note the transition from needle crystal to an essentially isotropic object as a result of increasing branching frequency.

for all. Nonetheless, processes leading to homogeneous secondary nucleation are expected to be associated with incomplete ordering of some kind, frozen into the crystal, i.e. analogous in essence to those discussed here.

4.5. *Formation of polycrystalline spherulites*

Spherulites are ubiquitous in solids formed under highly non-equilibrium conditions [23]. They are observed in a wide range of metallurgical alloys, in pure Se [7], in oxide and metallic glasses [37], mineral aggregates and volcanic rocks [38, 39], polymers [23, 40], liquid crystals [41], simple organic liquids [42], and diverse biological molecules [2, 43]. Many everyday materials, ranging from plastic grocery bags to airplane wings and cast iron supporting beams for highway bridges, are fabricated by freezing liquids into polycrystalline solids containing these structures. While the term 'spherulite' suggests a nearly spherical shape (circular shape in two dimensions where the term spherulite is still employed), this term is used in a broader sense of densely branched, polycrystalline solidification patterns. Spherulitic patterns exhibit a diversity of forms (see e.g. figure 1d–g).

Experimental studies performed over the last century indicate that there are two main categories of growth forms commonly termed spherulites [11]. Category 1 spherulites grow radially from the nucleation site, branching intermittently to maintain a space-filling character (figure 11). In contrast, Category 2 spherulites grow initially as thread-like fibres, subsequently forming new and new branches at the growth front (figure 11). This branching of the crystallization pattern ultimately leads to a crystal 'sheaf' that increasingly splays out during growth. At still longer times, these sheaves develop two 'eyes' (uncrystallized regions) on each side of the primary nucleation site. Ultimately, this type of spherulite settles down into a spherical growth pattern, with eye structures apparent in its core region. In some materials, both categories of spherulites occur in the same material under the same nominal thermodynamic conditions.

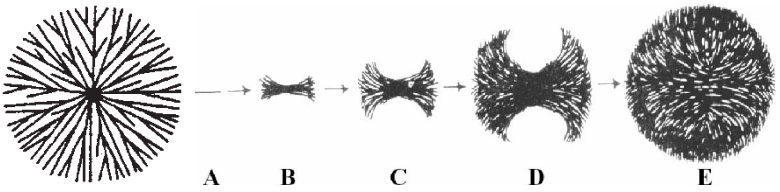

Figure 11. Concepts for the formation of category 1 and 2 spherulites. From left to right: Category 1 spherulite formed via central multidirectional growth. Formation of category 2 spherulite from a folded-chain single crystal (A) to the fully developed spherulite (E) via unidirectional growth and low angle branching [11]. Note that the latter mechanism may lead to the formation of two 'eyes' (uncrystallized holes) on the sides of the nucleation site.

Category 1 spherulites have been seen to form from transient single crystal nuclei [44]. Our model captures the gradual transition from square-shaped single crystals to circular-shaped under isothermal conditions. As seen in simulation, square-shaped single crystals nucleate after an initial incubation period. After exceeding a critical size (that depends on the ratio of the rotational and translational diffusion coefficients), the growing crystal cannot establish the same crystallographic orientation along its perimeter. The new grains form by a random version of the mechanism 'interface breakdown' suggested by Oldfield *et al.* [45]. The new grains are initiated by orientational defects frozen into the solid (figure 12). This process gradually establishes a circular perimeter for mature growth forms. Our simulations indicate that the formation of Category 1 spherulites may also start with the formation of polycrystalline nuclei consisting of multiple twins and other defects, a phenomenon known to happen even in metals [46] and simple model liquids [47]. Remarkably, similar patterns can also be obtained by branching with fixed branching angle at sufficiently large supersaturations (see rightmost column in figure 10).

Many studies of the early stages of the growth of Category 2 spherulites, especially in polymers, indicate that these structures initially grow as slender thread-like fibres [11, 23, 44, 48]. These structures successively branch to form a space-filling morphology. Our simulation with a fixed branching angle shown in the fourth column of figure 10 reproduces this phenomenon fairly well. A large kinetic anisotropy of twofold symmetry has been assumed, as is appropriate for polymeric systems that have a propensity to form crystal filaments. We included a preferred misorientation angle of 30° ($m = 3$ and $x = 0.15$). Ideally, in a system where filament branching happens with a 30° misfit, the polycrystalline growth form may consist of only grains that have six well-defined orientations (including the one that nucleated), which differ by multiples of 30°. With increasing driving force, the branching frequency increases, and more space-filling patterns emerge, while the average grain size decreases (figure 10). This leads to a continuous morphological transition that links the needle-crystals forming at low supersaturation to axialites, to crystal sheaves, and later to Category 2 spherulites (with 'eyes' on the two sides of the nucleus). With further increasing supersaturation the 'eyes' diminish and

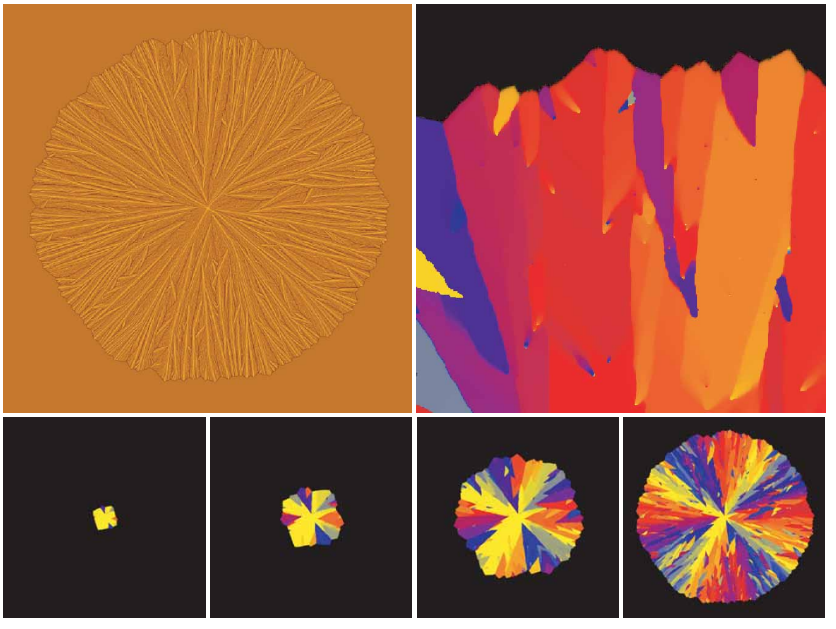

Figure 12. Formation of a Category 1 spherulite from a square-shaped single crystal via interface breakdown as predicted by the phase field theory. Upper row: composition map (left); magnified section of the orientation map of the interface (right). Lower row: snapshots of the orientation map. Time increases from left to right. Note the gradual morphological transition, and the lack of a sharp demarcation line between areas solidified with square and spherulitic morphology in the fully grown spherulite. With increasing size, the shape becomes more isotropic due to the randomizing effect of the newly formed grains. Note also the self-organized selection of grains whose maximum growth direction is perpendicular to the interface, yielding a cross-like pattern of grains with equivalent crystallographic orientations. (The simulation has been performed on a 4000×4000 grid. Snapshots taken at 1000, 2500, 5000, and 13 500 dimensionless time-steps, respectively are displayed. The left three panels show the central 2000×2000 section of the simulation, while fourth panel shows the full 4000×4000 simulation).

the Category 2 features gradually disappear, and we obtain eventually Category 1 spherulites.

The time evolution of a Category 2 spherulite is shown in figure 13. First, fibrils form and then secondary fibrils nucleate at the growth front to form crystal 'sheaves'. The diverging ends of these sheaves subsequently fan out with time to form eyes, and finally a roughly spherical growth form emerges. This progression of spherulitic growth is nearly universal in polymeric materials [11, 23, 44, 48].

Similar morphological evolution can be obtained via homogeneous secondary nucleation without preferred misorientation (i.e., random branching angle; see figure 14). Here – as in the case of Category 1 spherulites – frozen-in orientational defects initiate the branching of the fibres.

Summarizing, both homogeneous secondary nucleation mechanisms studied here (driven by quenched-in orientation defects and crystallographic branching with fixed misorientation) can produce Category 1 and Category 2 spherulites. Category 2 spherulites are expected in systems that grow crystal fibres, provided

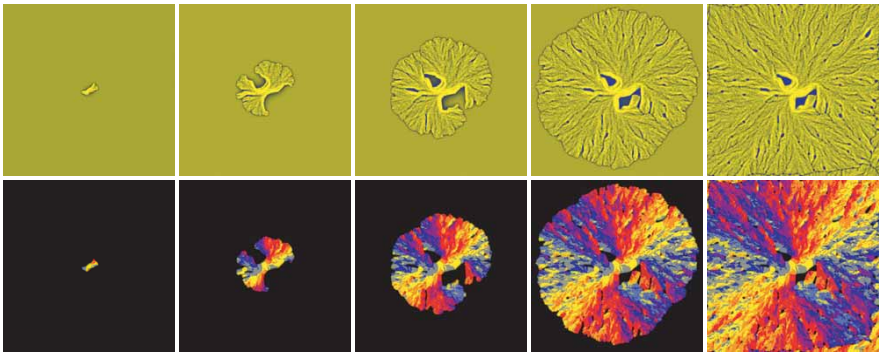

Figure 13. Time evolution of a Category 2 spherulite formed by random crystallographic branching as predicted by the phase field theory. The branching angle is 30°. Other conditions are as for the fourth column of figure 10. (Upper row: composition map; lower row: orientation map).

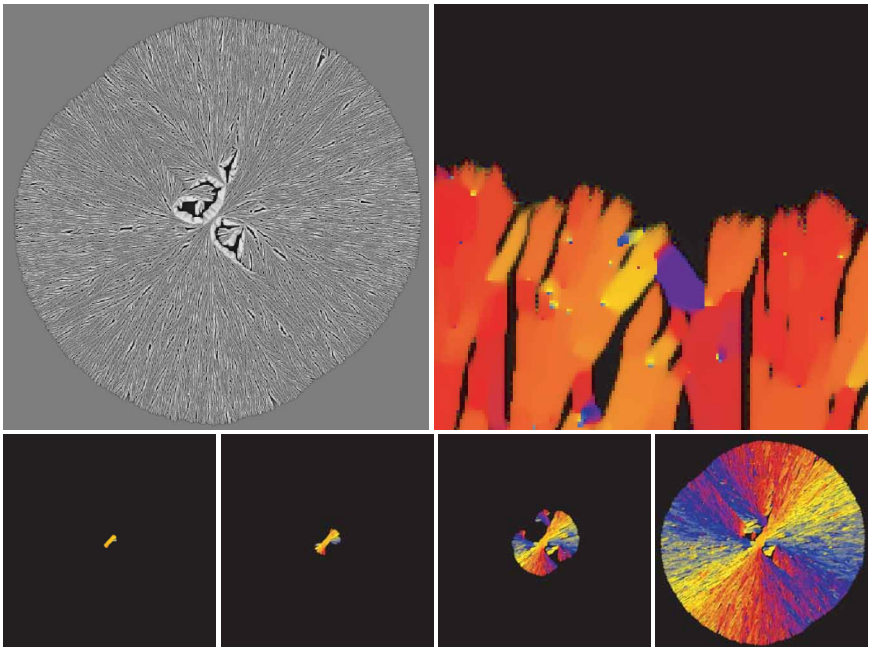

Figure 14. Formation of a Category 2 spherulite from a needle crystal via branching with random angle induced by trapped orientational disorder. Upper row: composition map (left); magnified section of the orientation map of the interface (right). Lower row: snapshots of the orientation map. Time increases from left to right. With increasing size, the shape becomes more isotropic due to the randomising effect of the newly formed filaments. (The simulation has been performed on a 2000×2000 grid. Snapshots taken at 500, 1000, 2500, and 7500 dimensionless time-steps are displayed).

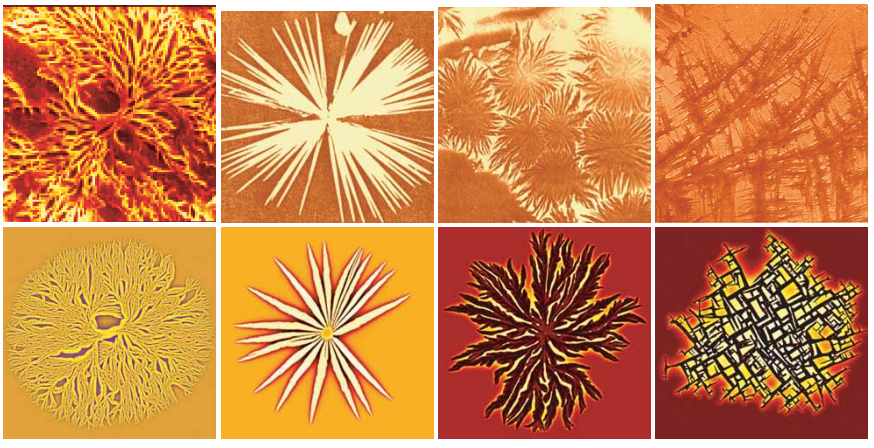

Figure 15. Polycrystalline spherulitic morphologies in experiment (upper row) and in the phase field theory (lower row). From left to right the experiments are from Wang *et al.* [50], Keith and Padden [51], Walker *et al.* [52] and Lotz and Wittmann [53]. In the lower row the contrast of the composition maps has been changed to match the experimental images. Diverse growth morphologies can be recovered varying only a few model parameters (anisotropies, branching angle, depth of metastable minimum).

that crystallization is initiated by single crystal nuclei. The coexistence of Category 1 and 2 spherulites has been reported in some systems. This can be understood if single crystal nuclei and multi-domain nuclei form parallel, a situation, which we have observed in our simulations at sufficiently low orientational mobilities.

Analysing the isothermal growth of Category 1 spherulites, we observed that, in agreement with experiment, the radial growth rate is constant. We investigated the time evolution of the crystalline fraction X for homogeneous primary nucleation of Category 1 spherulites under isothermal conditions on a 5000×5000 grid. We find that the transformation is well described by the Johnson–Mehl–Avrami–Kolmogorov model

$$X = 1 - \exp\left\{-[(t - t_0)/\tau]^p\right\}, \tag{7}$$

where t_0 is an incubation time due to the relaxation of the athermal fluctuation spectrum, τ is a time constant related to the nucleation and growth rates, and $p = 1 + d$ is the Avrami-Kolmogorov exponent, while d is the number of dimensions [49]. Fitting equation (7) to the simulation data between $0.01 < X < 0.95$ (where the data are the least noisy), we find $p = 3.04 \pm 0.02$ (and $\tau = 0.0106 \pm 0.00005$, $t_0 = 0.00178 \pm 0.00005$), which value is reasonably close to $p = 3$ expected for constant nucleation and growth rates in 2D [49].

These results imply that our phase field model captures many of the important features of spherulitic solidification.

Finally, we explore whether the morphological variability of spherulites can be recovered within the framework of our model. Figure 15 shows a selection of specific spherulitic morphologies and their theoretical counterparts. These simulations differ only in the driving force, anisotropies, branching angle, and mobilities, indicating

that the essential features of a broad variety of spherulitic morphologies can be captured, using only a few coarse-grained model parameters. Although the model parameters we use are unknown for most of these substances, and we have chosen them so that the particular morphology is reproduced, microscopic studies and atomistic simulations may give clues as to how these parameters should be chosen. For example, in the case of 'quadrites', the branching angle was known from visual inspection of the experimental images and from microscopic studies [11]. We expect, that as in the case of metallic dendrites [14], a parameter-free approach will become feasible in the future.

We conclude that rather complex solidification morphologies can be modelled using the phase field approach presented here. Work is underway to address the formation of spherulites and other complex morphologies in more detail [54].

5. Conclusions

The phase field model presented offers a general approach to polycrystalline solidification, and can be used to address a broad variety of processes including homogeneous and heterogeneous primary and secondary nucleation. In addition, a range of polycrystalline morphologies can be modelled, including disordered dendrites, spherulites, fractal-like aggregates, and many others.

Acknowledgements

The authors thank K. Lee and W. Losert, B.D. Nobel and P.F. James, V. Ferreiro, G. Faivre, D.C. Martin, F. Khoury, V. Fleury, C. Wang, A. Karim, and B. Lotz for the experimental images. This work has been supported by contracts OTKA-T-037323, ESA PECS Contract No. 98005, and by the EU FP6 Integrated Project IMPRESS, and forms part of the ESA MAP Projects No. AO-99-101 and AO-99-114. T.P. acknowledges support by the Bolyai János Scholarship of the Hungarian Academy of Sciences.

References

[1] G.W. Greenwood, A.L. Greer, D.M. Herlach, *et al*., Proc. Roy. Soc. Discussion Meeting on Nucleation Control, Trans. Roy. Soc. **361** 405 (2003).
[2] L.-W. Jin, K.A. Claborn, M. Kurimoto, *et al*., Proc. Natl. Acad. Sci. **100** 15297 (2003).
[3] K. Lee and W. Losert, 2004, personal communication.
[4] B.D. Nobel and P.F. James, 2003, personal communication.
[5] V. Ferreiro, J.F. Douglas, J.A. Warren, *et al*., Phys. Rev. E **65** 042802 (2002).
[6] V. Ferreiro, J.F. Douglas, J.A.Warren, *et al*., Phys. Rev. E **65** 051606 (2002).
[7] G. Ryshchenkow and G. Faivre, J. Cryst. Growth **87** 221 (1988).
[8] M. Ojeda and D.C. Martin, Macromol. **26** 6557 (1993).
[9] F.J. Padden and H.D. Keith, J. Appl. Phys. **36** 2987 (1965).
[10] H.D. Keith, F.J. Padden Jr. and R.G. Vadimsky, J. Polym. Sci. Part A-2 **4** 267 (1966).
[11] F. Khoury, J. Res. Natl. Bur. Stand. A **70** 29 (1966).
[12] V. Fleury, Nature **390** 145 (1997).

[13] W.J. Boettinger, J.A. Warren, C. Beckermann, *et al*., Ann. Rev. Mater. Res. **32** 163 (2002).
[14] J.J. Hoyt, M. Asta and A. Karma, Mater. Sci. Eng. Rep. R **41** 121 (2003).
[15] L. Gránásy, T. Pusztai and J.A. Warren J. Phys.: Condens. Matter **16** R1205 (2004).
[16] M. Castro, Phys. Rev. B **67** 035412 (2003).
[17] L. Gránásy, T. Börzsönyi and T. Pusztai, Phys. Rev. Lett. **88** 206105 (2002).
[18] K.R. Elder, F. Drolet, J.M. Kosterlitz, *et al*., Phys. Rev. Lett. **72** 677 (1994).
[19] F. Drolet, K.R. Elder, M. Grant and J.M. Kosterlitz, Phys. Rev. E **61** 6705 (2000).
[20] D. Lewis, T. Pusztai, L. Gránásy, *et al*., J. O. M. **56** 34 (2004).
[21] A. Roy, J.M. Rickman, J.D. Gunton, *et al*., Phys. Rev. E **56** 2610 (1998).
[22] L. Gránásy, T. Pusztai, G. Tóth, *et al*., J. Chem. Phys. **119** 10376 (2003).
[23] J.H. Magill, J. Mater. Sci. **36** 3143 (2001).
[24] L. Gránásy, T. Pusztai, T. Börzsönyi, *et al*., Nature Mater. **3** 645 (2004).
[25] L. Gránásy, T. Pusztai, J.A. Warren, *et al*., Nature Mater. **2** 92 (2003).
[26] R. Kobayashi and J.A. Warren, 2005, *Cond-mat/0502398*, submitted to *TMS. Lett*., presented at TMS Annual Meeting & Exhibition, San Francisco, 13–17 February, 2005.
[27] T. Pusztai, G. Bortel and L. Gránásy, Europhys. Lett. **71** 131 (2005).
[28] A. Karma and W.-J. Rappel, Phys. Rev. E **60** 3614 (1999).
[29] M. Plapp, 2002, personal communication.
[30] J.A. Warren and W.J. Boettinger, Acta Metall. Mater. **43** 689 (1995).
[31] M. Conti, Phys. Rev. E **56** 3197 (1997).
[32] A. Cacciuto, S. Auer and D. Frenkel, J. Chem. Phys. **119** 7467 (2003).
[33] R.L. Davidchack and B.B. Laird, Phys. Rev. Lett. **85** 4751 (2002).
[34] Y. Mu, A. Houk and X. Song, J. Phys. Chem. (2005), in print.
[35] G. Tóth, Diploma Thesis, Technical University of Budapest, Hungary (2004).
[36] S. Auer and D. Frenkel, Nature **409** 1020 (2001).
[37] P.F. James, *Advances in Ceramics*, Vol. 4, edited by J.H. Simmons, D.R. Uhlmann and G.H. Beagle (American Ceramics Society, Westerville (1982).
[38] H.W. Morse, C.H. Warren and J.D.H. Donnay, Am. J. of Sci. ser. 5 **23** 421 (1932).
[39] H.W. Morse and J.D.H. Donnay, Am. J. Sci., ser. 5 **23** 440 (1932).
[40] L.H. Sperling, *Introduction to Physical Polymer Science*, Chapter 6 (Wiley, New York, 1992).
[41] J.F. Hutter and J. Bechhoefer, J. Cryst. Growth **217** 332 (2000).
[42] J.H. Magill and D.J. Plazek, J. Chem. Phys. **46** 3757 (1967).
[43] P.J. Phillips, *Handbook of Crystal Growth*, Vol. 2, Chapter 18 (Elsevier, Amsterdam, 1993).
[44] J.H. Magill, J. Appl. Phys. **35** 3249 (1964).
[45] W. Oldfield, G.T. Geering and W.A. Tiller, *The Soldification of Metals* (Iron and Steel Inst. Publ., London, 1968) p. 110.
[46] M.H. Lee, P.J. Dobson and B. Cantor, *Mater. Res. Soc. Symp. Proc*., edited by R. Bormann *et al*., Vol. 400 (Mater. Res. Soc., Pittsburg, 1996), p. 95.
[47] B. O'Malley and I. Snook, Phys. Rev. Lett. **90** 085702 (2003).
[48] A. Keller and J.R. Waring, J. Polymer Sci. **17** 447 (1955).
[49] J.W. Christian, *The Theory of Transformation in Metals and Alloys* (Pergamon, Oxford, 1981).
[50] C. Wang, C.-C. Chen, Y.-W. Cheng, *et al*., Polymer **43** 71 (2002).
[51] H.D. Keith and F.J. Padden Jr. J. Appl. Phys. **34** 2409 (1963).
[52] M.L. Walker, A.P. Smith and A. Karim, Langmuir **19** 6582 (2003).
[53] B. Lotz, J.C. Wittmann, J. Polymer Sci.: Part B: Polymer Phys. **24** 1541 (1986).
[54] L. Gránásy, T. Pusztai, G. Tegze, J.A. Warren and J.F. Douglas, Phys. Rev. E. **72** 011605 (2005).